

# Bars in dark matter-dominated dwarf galaxy discs

A. Marasco,<sup>1</sup><sup>\*</sup> K. A. Oman,<sup>2</sup> J. F. Navarro,<sup>2,3</sup> C. S. Frenk<sup>4</sup> and T. Oosterloo<sup>1,5</sup>

<sup>1</sup> *ASTRON, Netherlands Institute for Radio Astronomy, Postbus 2, 7900 AA, Dwingeloo, The Netherlands*

<sup>2</sup> *Department of Physics & Astronomy, University of Victoria, Victoria, BC, V8P 5C2, Canada*

<sup>3</sup> *Senior CIFAR Fellow*

<sup>4</sup> *Institute for Computational Cosmology, Department of Physics, University of Durham, South Road, Durham DH1 3LE, United Kingdom*

<sup>5</sup> *Kapteyn Astronomical Institute, University of Groningen, Postbus 800, 9700 AV Groningen, The Netherlands*

Accepted XXX. Received YYY; in original form ZZZ

## ABSTRACT

We study the shape and kinematics of simulated dwarf galaxy discs in the APOSTLE suite of  $\Lambda$ CDM cosmological hydrodynamical simulations. We find that a large fraction of these gas-rich, star-forming discs show weak bars in their stellar component, despite being dark matter-dominated systems. The bar pattern shape and orientation reflect the ellipticity of the dark matter potential, and its rotation is locked to the slow figure rotation of the triaxial dark halo. The bar-like nature of the potential induces non-circular motions in the gas component, including strong bisymmetric flows that can be readily seen as  $m=3$  harmonic perturbations in the H I line-of-sight velocity fields. Similar bisymmetric flows are seen in many galaxies of the THINGS and LITTLE THINGS surveys, although on average their amplitudes are a factor of  $\sim 2$  weaker than in our simulated discs. Our results indicate that bar-like patterns may arise even when baryons are not dominant, and that they are common enough to warrant careful consideration when analyzing the gas kinematics of dwarf galaxy discs.

**Key words:** galaxies: structure – galaxies: kinematics and dynamics – galaxies: dwarf – ISM: kinematics and dynamics – dark matter

## 1 INTRODUCTION

Bars are a common morphological feature of spiral galaxies in the local Universe. About one-quarter of disc galaxies show strong bars (Masters et al. 2011; Cheung et al. 2013), and this fraction increases up to about two-thirds when including weaker features (Mulchaey & Regan 1997; Kormendy & Kennicutt 2004). The fraction of barred galaxy appears to depend significantly on galaxy luminosity, being lower for fainter galaxies (Méndez-Abreu et al. 2010; Janz et al. 2012), and, to a minor extent, on environment, increasing in regions of higher galaxy density (Méndez-Abreu et al. 2012).

Bars have been a topic of interest for decades, and numerical simulations have played a major role in our current understanding of their formation and evolution. Although details need to be fully worked out, there is widespread agreement that bars develop in stellar discs as a consequence of the inevitable tendency of collisionless systems to evolve dynamically by redistributing mass inwards and angular momentum outwards.

Bar patterns offer a particularly efficient way of carrying out this redistribution, and grow and strengthen rapidly in

cold, massive stellar discs (see, e.g., Athanassoula 2013; Sellwood 2014, for recent reviews). Their growth is so rapid in such systems (Miller & Prendergast 1968; Hockney & Hohl 1969) that few can avoid becoming ‘bar unstable’ in a couple of rotation periods (Sellwood & Wilkinson 1993), unless stabilized by the presence of a dominant dark halo (Ostriker & Peebles 1973). These results have been so influential that the presence of bar-like patterns is often taken to indicate discs where the dark halo is gravitationally unimportant; i.e., discs that are ‘maximal’.

More recent work, however, suggests a more complex scenario where bar formation is delayed, but not fully inhibited, in discs where dark matter haloes are gravitationally dominant (e.g., Athanassoula 2002, 2003; Algorry et al. 2017): bars are thus not synonymous with maximal discs, suggesting that care must be exercised when using morphological features to infer indirectly the relative importance of disc and halo in spiral galaxies.

Bars are not the only bisymmetric ( $m=2$ ) perturbation expected in disc galaxies. Indeed, discs are expected to form at the centre of cold dark matter (CDM) haloes, which have long been known to be triaxial in nature (Frenk et al. 1988; Warren et al. 1992; Jing & Suto 2002). Discs that settle on the symmetry plane of such haloes would be subject to gravitational forces akin to those in barred systems, although the

\* marasco@astron.nl

bisymmetric pattern in this case is expected to rotate much less rapidly than in typical strongly-barréd systems.

The consequences of halo triaxiality on the kinematics of discs have not been extensively studied (although see [Hayashi et al. 2007](#), for an attempt), in part because the assembly of the disc is thought to ‘sphericalise’ the halo (see [Abadi et al. 2010](#), and references therein). However, this is only true in the case of massive discs such as those of luminous, high surface brightness spirals. In the case of fainter, lower surface brightness spirals, discs are less gravitationally important and the sphericalisation of their surrounding haloes should be less complete ([Machado & Athanassoula 2010](#); [Kazantzidis et al. 2010](#)).

Regardless of origin, bar-like perturbations can have important consequences on the kinematic of discs, particularly on the interpretation of azimuthally-averaged rotation curves and of 2D velocity fields of gas and stars. [Hayashi & Navarro \(2006, hereafter HN06\)](#), for example, showed that even minor deviations from spherical symmetry can induce large deviations from circular orbits in the velocity field of a gaseous disc. This possibility was studied by [Trachternach et al. \(2008\)](#), who carried out a harmonic decomposition of the HI velocity fields in 19 galaxies from The HI Nearby Galaxy Survey (THINGS, [Walter et al. 2008](#)). The harmonic decomposition suggests that the magnitude of non-circular motions in the central regions of these systems is small, and compatible with a circularly-symmetric potential.

However, most of the systems studied by [Trachternach et al.](#) were large spirals, and the analysis has not been extended to the dwarf galaxy regime, where the triaxiality of the halo might be better preserved. A harmonic decomposition of LITTLE THINGS galaxies ([Hunter et al. 2012](#)) was performed by [Oh et al. \(2015\)](#), but their findings were not discussed in terms of triaxiality of the gravitational potential, thus whether or not dwarf galaxies are consistent with hosting triaxial halos is still an open question.

Recently, [Oman et al. \(2017, hereafter O17\)](#) have studied the gas kinematics in a sample of 33 simulated dwarf galaxies from the APOSTLE suite of  $\Lambda$ CDM cosmological simulations ([Sawala et al. 2015](#); [Fattahi et al. 2016](#)). Their approach used synthetic HI observations of these systems, from which the gas rotation curve was derived using the same tilted ring modelling technique adopted in most HI observational studies.

One of the main results of O17 is that, depending on the orientation of the line of sight, a large variety of rotation curves might be derived for the same system, even for fixed inclination. The variety is due to non-circular motions in the gas; in particular, to strong bisymmetric ( $m = 2$  harmonic) fluctuations in the azimuthal HI velocity field, which the tilted-ring model is not well suited to account for. We study here the origin of these non-circular motions, focussing on the mass distribution and the shape of the gravitational potential. We show that the cause of these bisymmetric gas flows is the presence of bar-like features in both the stellar and the dark matter distributions.

This paper is structured as follows. In Section 2 we summarise the main features of the APOSTLE simulations and of the selected galaxy sample. In Section 3 we discuss the properties of the stellar and dark matter bars in our sample, and how they affect the gas kinematics. A comparison with dark-matter-only simulations and with the observations is

also presented. We finally summarise our findings in Section 4.

## 2 SIMULATIONS AND SAMPLE SELECTION

A detailed description of the APOSTLE<sup>1</sup> simulations can be found in [Sawala et al. \(2015\)](#) and [Fattahi et al. \(2016\)](#). Here, we summarise their main characteristics.

APOSTLE is a suite of cosmological hydrodynamical simulations performed in a  $\Lambda$ CDM framework, adopting the cosmological parameters inferred from WMAP-7 data ([Komatsu et al. 2011](#)). It consists of 12 subvolumes selected from the DOVE cosmological simulation ([Jenkins 2013](#)) and re-simulated using the zoom-in technique ([Frenk et al. 1996](#); [Power et al. 2003](#)). The volumes are centred around two massive haloes (analogous to the Milky Way - M31 pair) and chosen to resemble these galaxies in terms of mass, separation and kinematics, whilst ensuring relative isolation from more massive structures.

The hydrodynamics and the baryonic subgrid physics implemented in APOSTLE are the same as those adopted in the EAGLE simulations ([Schaye et al. 2015](#); [Crain et al. 2015](#)). EAGLE, and by extension APOSTLE, uses a formulation of the smoothed-particle hydrodynamics (SPH) known as ANARCHY ([Dalla Vecchia in prep](#), see also Appendix A of [Schaye et al. 2015](#)), which alleviates significantly the issues related to artificial gas clumping and the poor treatment of hydrodynamical instabilities associated with the classical SPH scheme (e.g [Kaufmann et al. 2006](#); [Agertz et al. 2007](#)). Other features introduced by ANARCHY are the use of an artificial viscosity switch ([Cullen & Dehnen 2010](#)), an artificial conduction switch ([Price 2008](#)) and a timestep limiter ([Durier & Dalla Vecchia 2012](#)). The recipes for subgrid physics include the star formation implementation of [Schaye & Dalla Vecchia \(2008\)](#), thermal star formation feedback from [Dalla Vecchia & Schaye \(2012\)](#), radiative gas cooling and photo-heating from [Wiersma et al. \(2009a\)](#) and stellar mass loss from [Wiersma et al. \(2009b\)](#). Accretion onto black holes and AGN feedback is not implemented in APOSTLE but this is not critical for the mass scale of interest.

The APOSTLE volumes are resimulated at three levels of resolution. As in O17, here we focus on the highest resolution level (‘L1’ in [Fattahi et al. 2016](#)), featuring a dark matter particle mass of  $3.6 \times 10^4 M_{\odot}$ , a gas particle initial mass of  $7.4 \times 10^3 M_{\odot}$  and maximum softening length of 134 pc. At the moment of writing, only five of the 12 volumes have been re-simulated at this resolution. Galaxies, and in general ‘subhaloes’, are identified in the simulation via the SUBFIND algorithm ([Dolag et al. 2009](#)), which is based on a friend-of-friends (FoF) scheme.

O17 studied 33 dwarf systems, selecting central<sup>2</sup> subhaloes with maximum circular velocity  $60 < V_{\max} < 120 \text{ km s}^{-1}$  at redshift  $z=0$ . The  $V_{\max}$  selection targets the ‘dwarf’ spiral regime, while the exclusion of satellites allows us to discard systems whose features might be affected by the effect of tides.

We focus here on the same galaxy sample, whose main

<sup>1</sup> A Project Of Simulating The Local Environment

<sup>2</sup> A ‘central’ subhalo is the most massive subhalo of each FoF group, and is therefore not a satellite of a more massive system.

properties are listed in Table A1 of O17. Each simulated galaxy is uniquely identified by four labels: the resolution level (always L1 in our sample), the APOSTLE volume it belongs to (V1, V2,..., V12), the FoF group, and SUBFIND sub-group numbers, respectively. The latter is always equal to 0, indicating that the system is the central subhalo of its FoF group. These labels follow the ‘AP’ keyword that identifies the suite of simulations used.

As in other studies of neutral hydrogen using the EA-GLE simulations, the HI mass fraction of each gas particle in the APOSTLE volumes is computed in two steps: the fraction of neutral hydrogen is first derived following the prescription of Rahmati et al. (2013) for self-shielding from the meta-galactic ionising background, and then a pressure-dependent correction for the molecular gas fraction is applied following Blitz & Rosolowsky (2006). We refer the interested reader to Crain et al. (2017) for details.

### 3 RESULTS

#### 3.1 Stellar bars and ‘dark bars’

For illustration, we present first the mass distribution and the HI kinematics in the inner regions of two representative systems in the sample of O17: AP-L1-V10-19-0 and AP-L1-V10-17-0. These systems have comparable  $V_{\max}$  (67 and  $65 \text{ km s}^{-1}$  respectively), stellar mass ( $4.7$  and  $7.1 \times 10^8 M_{\odot}$ ), HI-to-stellar mass ratio (1.1 and 0.7) and star formation rates at  $z = 0$  ( $0.08$  and  $0.13 M_{\odot} \text{ yr}^{-1}$ ). Also, both systems are quite isolated, lying at more than 2 Mpc from the closest member of the Milky Way/M31 analog pair. They also show no obvious sign of interactions with nearby galaxies.

Fig. 1 shows a series of face-on maps for these two galaxies, where the rotation axis of the galaxy is identified with  $\vec{L}_*$ , the angular momentum vector of all stars (identified by SUBFIND as bound to the system and located within a radius enclosing 90 per cent of the total stellar mass) relative to the galaxy centre. The latter is defined as the location of the particle with the lowest potential energy. All maps are smoothed to a spatial resolution (FWHM of a Gaussian kernel) of 0.2 kpc.

The leftmost two panels of Fig. 1 show the stellar and dark matter surface density maps derived projecting a cubic region with side-length 8 kpc, concentric with the galaxy. The elongation of the isodensity contours reveals that *both* stars and dark matter are clearly non-axisymmetric. Projected onto the disc plane, both components seem bar-like, especially in the central few kiloparsecs. For simplicity, we will refer to these non-axisymmetric features as the ‘stellar’ bar and the ‘dark’ bar.

These two ‘bars’ have the same orientation and, approximately, the same axis ratio. The central panels show isopotential contours measured on the disc midplane, computed using all (dark + baryonic) particles identified by SUBFIND as bound to the system (the gravitational potential,  $\Phi$ , is softened on scales smaller than 100 pc). The gravitational potential is clearly aspherical, especially close to the centre, and is therefore expected to induce deviations from pure circular rotation in the motion of gas and stars in the disc.

These deviations are explored in the rightmost two panels, which show the azimuthal and the radial HI velocity

fields derived on the galaxy midplane, from which we have subtracted the mean azimuthally averaged value at each radius. If the gas was in pure circular rotation around the centre, these ‘residual’ velocity fields should not show systematic deviations from zero. Instead, clear  $m=2$  harmonic patterns are visible, which were already noticed by O17 in other systems of the sample.

The phase of the  $m = 2$  perturbation in the azimuthal velocity (shown by the black crosses in the fourth column of Fig. 1, which trace the maximum positive deviation from the mean) is oriented approximately perpendicular to the major axis of the potential (dashed black line, see below), whereas the phase of the perturbation in the radial velocity lags  $45^\circ$  from the latter. This pattern is consistent with gas moving counter-clockwise along elliptical orbits elongated in the same direction of the potential. The simplest interpretation of these orbits is that, in these galaxies, the stellar/dark bar induces a bisymmetric flow in the gas component.

We determine major and minor axes for the bar by fitting an ellipse to the surface density contour whose semi-major axis coincides with  $R_{\text{h}}$ , the (projected) stellar half-mass radius. This is highlighted in blue in the leftmost panels of Fig. 1. The ellipse centre is a free parameter of the fit, in order to account for possible offsets in the mass distribution.  $R_{\text{h}}$  is computed directly from the face-on stellar density distribution.

#### 3.2 Stellar bars in sub-dominant discs

The two leftmost panels of Fig. 1 suggest that the dark matter dominates the dynamics in the central few kiloparsecs. This is shown explicitly in the top panels of Fig. 2 which show, for both systems, the gravitational acceleration due to the stars alone (orange lines) and to the dark matter (blue lines) on the galactic midplane along the projected major (dashed lines) and minor (solid lines) axes of the bar. The gas contribution to the gravitational acceleration is negligible compared to the other components.

Fig. 2 clearly indicates that, in these two systems, the overall dynamics is dominated everywhere - even at the very centre - by the dark matter. This suggests that, in these two systems, the stellar bar originates as a response to the non-axisymmetric distribution of dark matter, and not, as traditionally envisioned, as a result of some instability in a stellar-dominated disc. At least some stellar bars can, therefore, form in non-maximal discs, provided they are embedded in triaxial dark matter halos.

One may wonder whether the alignment of the dark and the stellar ‘bars’ shown in Fig. 1 is fortuitous, or if it is also present at earlier times. We use the APOSTLE particle data at redshift  $z > 0$  to follow the evolution of these two galaxies in the previous 1.5 Gyr. At each time-step, new surface density maps - analogous to those of Fig. 1 - are produced by projecting the system particles for a face-on view using the same  $\vec{L}_*$  determined at  $z=0$ . Note that this technique fails if the galactic plane rotates with time, but this is not the case for the systems considered here.

As before, we fit the  $R_{\text{h}}$  iso-contour of these maps with an ellipse to determine the axis ratio and the orientation of both ‘bars’. The middle panels of Fig. 2 show the phases of the stellar (circles) and of the dark (squares) bars as a function of the lookback time for both galaxies. The bars are

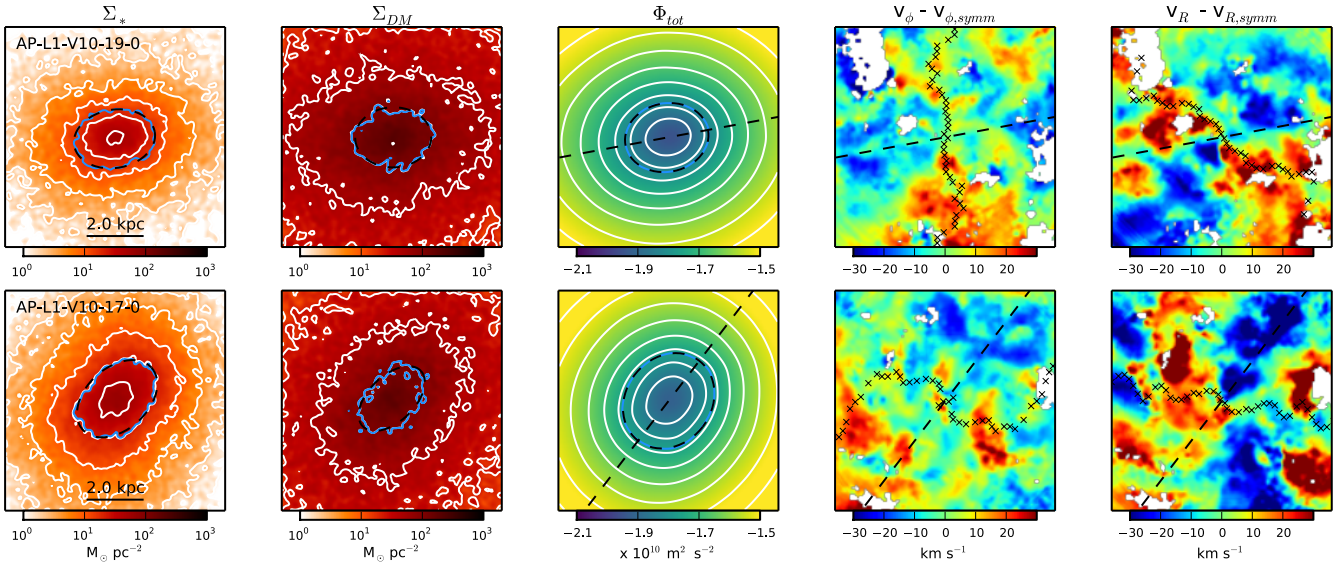


**Figure 1.** Face-on maps of two representative APOSTLE dwarfs at redshift 0. *First and second columns:* stellar and dark matter surface density maps, shown on the same colour scale. Isodensity contours (in white) are spaced by 0.3 dex. The blue isodensity contour has semi-major axis equal to the projected radius at half stellar mass,  $R_h$ ; the dashed black line shows the best-fit ellipse to this contour. *Third column:* gravitational potential map on the galactic midplane. *Fourth and fifth columns:* maps of the azimuthal and radial HI velocity fields, also on the midplane, from which we have subtracted the mean velocity computed at different radii. A residual  $m=2$  mode is clearly visible in both maps; its phase is traced by black crosses. The dashed black line in the rightmost three panels shows the major axis of the gravitational potential.

clearly locked in phase and rotate very slowly with pattern speeds of less than  $1 \text{ km s}^{-1} \text{ kpc}^{-1}$ . As we show in Section 3.3, this is typically the case for barred dwarf galaxies in the APOSTLE simulations.

We can quantify the magnitude of the perturbations in the gravitational potential induced by the bars via a harmonic analysis of the  $\Phi$  map shown in Fig. 1. For this purpose, we divide the  $\Phi$  map into a series of concentric rings of increasing radius, each centred at the minimum of the potential and with thickness equal to 100 pc. The values of  $\Phi$  as a function of the azimuthal angle  $\theta$  are fit, for each ring separately, with

$$\Phi(\theta) = \sum_{m=0}^3 A_m \cos(m\theta - \theta_m), \quad (1)$$

which is a harmonic expansion of the potential up to third order.

The bottom panels of Fig. 1 show, as a function of  $R$ , the ratio between the amplitudes  $A_m$  of the  $m > 0$  modes and the mean value of  $\Phi$  at each radius (i.e., the  $m = 0$  mode amplitude). As expected, the strongest perturbation mode is the  $m = 2$ , which reaches amplitudes of  $\sim 0.01 \times A_0$  at  $R = R_h$  (black arrows). Perturbations of order  $m = 3$  are virtually negligible, whereas  $m = 1$  perturbations are intermediate. Even though the overall fluctuations in the potential are only of a few per cent, they are enough to affect significantly the gas velocity field, as discussed by HN06.

We note that, while in the models of HN06 the gas follows elliptical closed orbits with major axis oriented perpendicularly to the bar, in the two systems studied here the major axis of the potential and that of the gas orbits are aligned. We find that this is the case for the majority of our

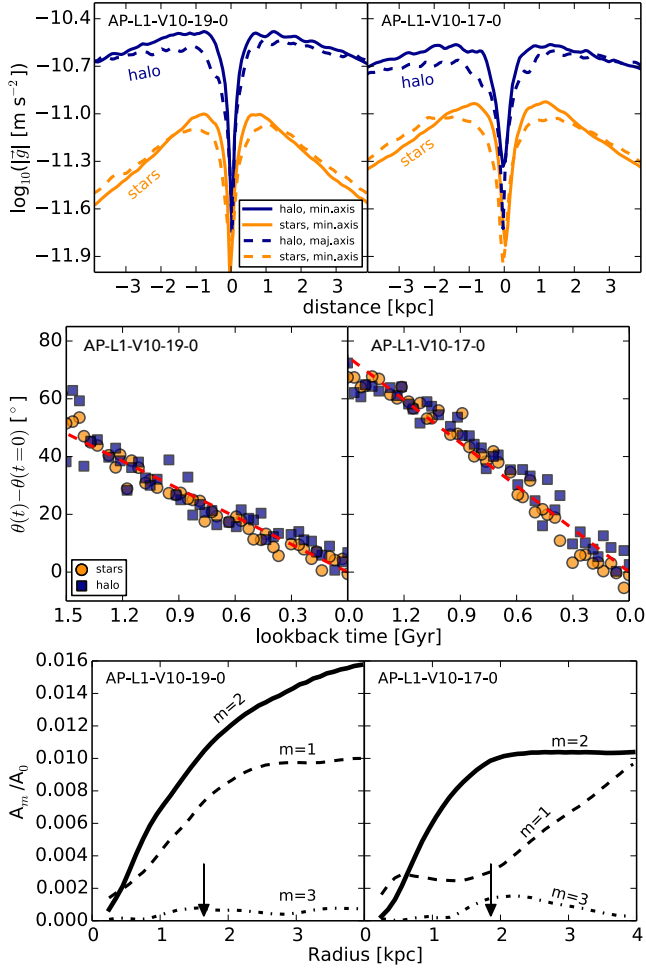
simulated dwarfs, although the alignment is not always as clean as in AP-L1-V10-19-0 and AP-L1-V10-17-0.

There are several differences between our galaxies and those in the HN06 models. The first is that the bars in our systems slowly rotate with time, while they were steady in HN06. The orientation of the closed orbits in a rotating barred potential depends on the positions of the inner Lindblad resonance and of the co-rotation radius, which vary from case to case depending on the exact shape and pattern speed of the potential (e.g. Contopoulos & Grosbol 1989; Athanassoula 1992; Sellwood & Wilkinson 1993). A second difference is that the HN06 models are based on the epicycle approximation, which breaks down when perturbations in the velocity field exceed a few per cent - they are typically of order  $\sim 25$  per cent at the half-mass radius in the cases we consider here. Finally, in our galaxies the gas does not settle exactly on closed orbits but slowly flows inwards with time, as we verified by following the trajectories of a sample of gas particles in the two APOSTLE systems studied here. Overall, the APOSTLE dwarfs are more complex than the simple systems considered by HN06. A detailed analysis of the orbits of their gas and star particles is planned for a future study.

### 3.3 General properties of stellar and dark bars

We now extend the previous analysis to the entire sample of 33 simulated dwarf galaxies studied by O17. These systems are selected to have  $60 < V_{\text{max}} / \text{km s}^{-1} < 120$ , and typically have  $M_{\text{HI}}$  comparable to  $M_*$  (see Table A1 in O17).

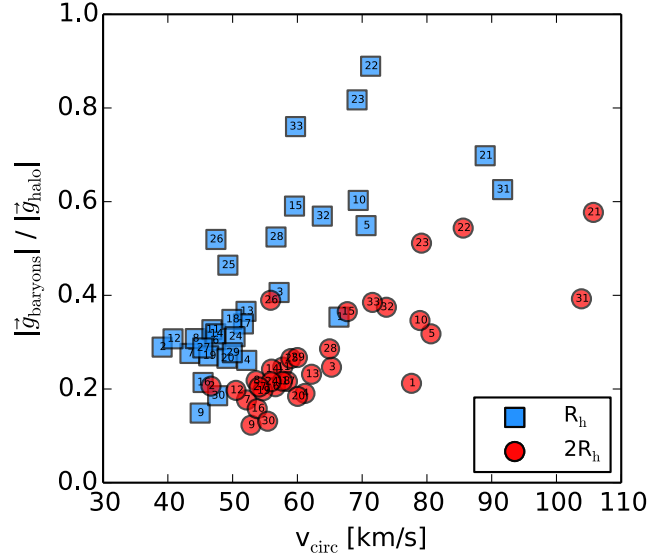
The dynamics of each system in this sample are dominated everywhere by the dark matter. This is shown in



**Figure 2.** *Top panels:* gravitational acceleration on the galactic midplane decomposed into contributions from stars (orange lines) and from dark matter (blue lines) as a function of the distance along the major axis (dashed lines) or the minor axis (solid lines) of the bar for the two representative galaxies. Dark matter dominates the gravitational acceleration within the bar. *Central panels:* phases of the stellar (orange circles) and of the dark matter (blue squares) bar as a function of the lookback time. Phases are locked. *Bottom panels:* amplitude of the  $m > 0$  harmonic fluctuations in the gravitational potential  $\Phi$ , divided by the mean value of  $\Phi$ , as a function of  $R$ . The strongest harmonic mode is the  $m=2$ . The arrows show the location of  $R_h$ .

Fig. 3, where we plot the ratio of the midplane gravitational acceleration contributed by baryons and by the dark matter, respectively, as a function of the circular velocity,  $V_{\text{circ}}$ . We show the ratios computed at  $R=R_h$  (squares) and at  $R=2R_h$  (circles).

A clear trend is visible: the larger  $V_{\text{circ}}$  is, the higher the contribution of the baryons to the total acceleration. However, in all cases, the baryons are subdominant: their contribution to the total acceleration ranges from 10% to 90% of that given by the dark matter alone, decreasing towards the outer regions of the galaxies. Interestingly, by extrapolation of the trend shown in Fig. 3, it is clear that the baryons *will* dominate the central dynamics in galaxies more massive than those studied here (see also Schaller et al. 2016).



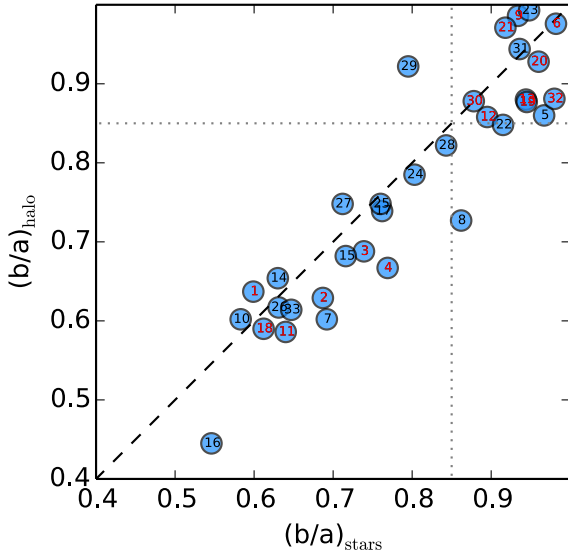
**Figure 3.** Ratio between the baryonic and the dark matter gravitational acceleration on the midplane as a function of the circular velocity  $\sqrt{GM(<R)}/R$  computed at  $R=R_h$  (squares) and at  $R=2R_h$  (circles) for the simulated dwarfs. Baryons are always subdominant.

Fig. 4 compares the axis ratio of the stellar bar with that of the dark bar for all systems in the sample. As before, the axis ratios are determined by fitting ellipses to the highest contour passing by  $R_h$  in face-on surface density maps. For the vast majority of systems, the two axis ratios are very similar, suggesting again that the origin of the stellar bars is closely linked to non-axisymmetries in the dark matter. The symbol numbers in Fig. 4 label the various systems as in Table A1 of O17.

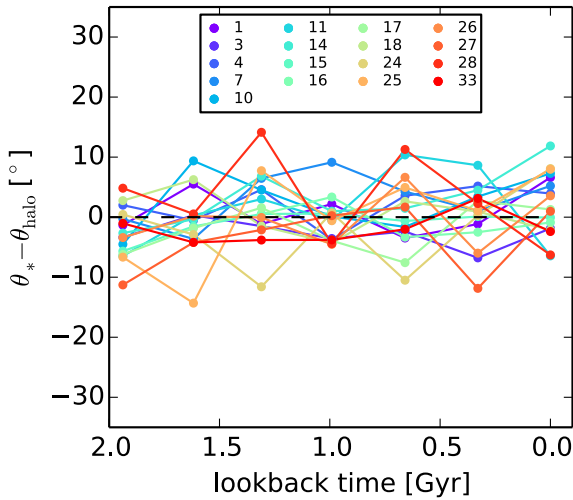
We define a ‘barred’ subsample of 18 galaxies (55% of the sample) by selecting those systems with axis ratio smaller than 0.85 for both the stellar and the dark matter components. This threshold is chosen because we found it impossible to track a bar backwards in time when its axis ratio is rounder than 0.85. Numbers in red in Fig. 4 are used to identify the subsample of 14 dwarfs identified by O17 as being ‘in equilibrium’: these are galaxies where the HI average azimuthal speed, computed at  $R=2\text{ kpc}$ , matches the circular velocity at the same radius. In general, there is a tendency for these systems to have a large axis ratio, suggesting that galaxies whose halo is more spherical are, according to that definition, closer to dynamical equilibrium than more strongly barred systems.

Fig. 5 shows how the difference between the phase of the stellar bar and that of the dark bar evolves in time. In all cases, the phase difference remains below  $\sim 15^\circ$  in the 2 Gyr before the present time, confirming that the stellar and dark bars always rotate in phase, and with the same pattern speed. Note that the system labelled as ‘2’ is missing in Fig. 5: a close encounter occurring at the lookback time of  $\sim 0.5\text{ Gyr}$  unsettled the stellar disc and made it difficult to follow the evolution of the bar at earlier epochs.

We now analyse the strength and the pattern speed of the stellar bars in our sample. Following Algorry et al. (2017), we define the strength of the stellar bar by measur-



**Figure 4.** Stellar bar versus halo bar axis ratio for our simulated dwarfs. Systems are numbered as in Table A1 of O17, with numbers in red representing galaxies ‘in equilibrium’ (see text). 55 per cent (18/33) of galaxies have axis ratios smaller than 0.85 and constitute our ‘barred’ subsample.



**Figure 5.** Difference between the phase of the stellar bar and the phase of the halo bar as a function of the lookback time for our subsample of simulated barred dwarfs. Systems are numbered as in Table A1 of O17. Phases are always locked.

ing the amplitude of the  $m=2$  Fourier mode of the azimuthal distribution of star particles. Specifically, we compute

$$a_m(R) = \sum_{i=1}^{n_R} m_i \cos(m\phi_i); \quad b_m(R) = \sum_{i=1}^{n_R} m_i \sin(m\phi_i) \quad (2)$$

where  $m_i$  is the mass of the  $i$ -th star particle and the sum is extended to all  $n_R$  particles that occupy a given cylindrical annulus with mean radius  $R$ . We then define  $A_{2,*}(R) = \sqrt{a_2^2 + b_2^2}/a_0$ , and the strength of the bar as  $A_{2,*}^{\max} = \max(A_{2,*}(R))$ .

The distribution of  $A_{2,*}^{\max}$  is shown in the left panel of Fig. 6. All systems have bar strength below 0.4, which im-

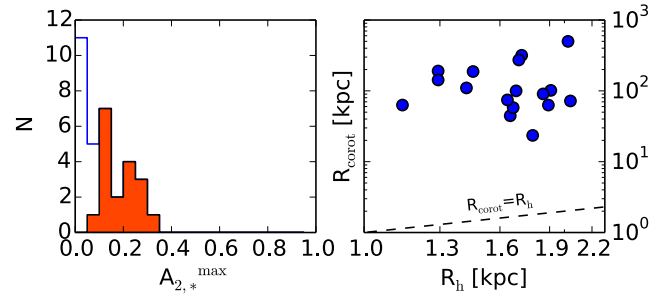


**Figure 6.** Properties of stellar bars in our simulated dwarfs. *Left panel:* strength of the bar,  $A_{2,*}^{\max}$  (see text), for the full sample (unfilled histogram) and for the barred subsample (filled histogram). *Right panel:* bar co-rotation radius plotted against the projected radius at half stellar mass. The dashed line shows the one-to-one relation.

plies that they are all ‘weak bars’ according to the criterion of [Algorry et al. \(2017\)](#), with only 7 systems with  $0.2 < A_{2,*}^{\max} < 0.4$ . In the right panel of Fig. 6 we compare the bar co-rotation radius,  $R_{\text{corot},*}$ , and  $R_h$  in our subsample of barred galaxies.  $R_{\text{corot},*}$  is determined by first computing the bar pattern speed,  $\Omega_*$ , and then by equating  $\Omega_* R$  to the circular velocity of the system,  $\sqrt{GM(< R)}/R$ .  $\Omega_*$  is computed by fitting with a straight line the trend of the phase of the stellar bar with time, from lookback times of 2 Gyr to the present day. We find that  $\Omega_*$  is typically smaller than  $1 \text{ km s}^{-1} \text{ kpc}^{-1}$ , and the corresponding co-rotation radii  $R_{\text{corot},*}$  always exceed by far the system sizes.

All stellar bars in our sample are relatively weak, very slowly rotating, and most likely originate from the triaxial structure of their dominant dark matter haloes.

### 3.4 Baryons and halo triaxiality

As discussed in Sec. 1, the assembly of the baryonic component of a galaxy is expected to sphericalise the dark matter distribution. If so, this process has only gone to partial completion in APOSTLE dwarfs, given the prevalence of non-axisymmetric features (‘dark bars’) in our galaxy sample. We examine this question by studying the properties of 14 subhaloes with  $60 < V_{\text{max}} < 120 \text{ km s}^{-1}$  extracted from volumes AP-L1-V1 and AP-L1-V4 in the APOSTLE dark-matter-only (DMO) simulations, which are the DMO counterparts of the corresponding full hydrodynamical runs.

By analogy with our previous analysis, we measure deviations from axisymmetry by computing the axis ratio of face-on isodensity contours with semi-major axis length of 1.7 kpc, corresponding to the median  $R_h$  in our original sample. Since DMO runs have no stars, we define the face-on projection axis as the minor axis of the inertia tensor of all dark matter particles within 8 kpc from the halo centre. For consistency, we repeat the same procedure for our original sample of 33 galaxies in the hydrodynamical runs, so that dark matter axis ratios are derived in the same way for the two samples.

In Fig. 7 we compare the  $b/a$  distributions for the dark matter in the hydrodynamical (full histogram) and in the DMO (dashed histogram) samples. Even though the sample is small, it is clear that deviations from axisymmetry are

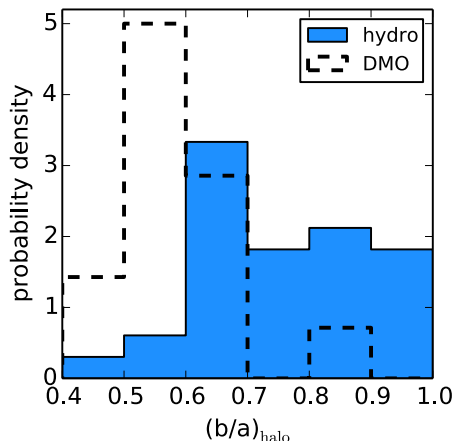


**Figure 7.** Axis ratio distribution for the dark bars in our sample of simulated dwarfs (filled histogram) and in a sample of subhaloes with  $60 < V_{\max} < 120 \text{ km s}^{-1}$  from the APOSTLE dark-matter-only simulations (dashed histogram). Dark bars in dark matter-only runs have lower axis ratio.

more pronounced in the DMO case than in the hydro simulations. As expected, the assembly of baryons at the centre of a halo reduces, but does not erase, the triaxiality of the potential in the innermost few kpc, in line with the findings of Kazantzidis et al. (2010); Abadi et al. (2010); Machado & Athanassoula (2010).

### 3.5 Comparison with observations

We now compare the amplitude of the harmonic perturbations in the HI velocity fields of real galaxies with those found in our simulations. For the latter, we use the same sample of 43 dwarfs (17 from THINGS, 26 from LITTLE THINGS) already considered by O17, adopting the ‘natural’-weighted moment-1 maps of these galaxies. These observations have angular resolution of  $\sim 12''$ , corresponding to a median spatial resolution of order  $\sim 250 \text{ pc}$ . The overall kinematics of these systems has been already studied and reported by de Blok et al. (2008) and Oh et al. (2015).

In observed galaxies we do not have access to the 3D velocity field, but only to its projection along the line-of-sight. As is well known (e.g. Schoenmakers et al. 1997; Spekkens & Sellwood 2007), harmonic perturbations of order  $m$  in the azimuthal or radial velocity field produce harmonic distortions of orders  $m' = m \pm 1$  in the line-of-sight velocity field. Hence a bisymmetric flow in real space produces an  $m' = 1$  and an  $m' = 3$  perturbations in projected space, both having similar amplitude.

While the former is difficult to detect, as its signal blends with that produced by the regular rotation of the disc, the latter is a unique signature of bisymmetric flows and can be readily studied via a harmonic decomposition of the velocity field. Our strategy is therefore to produce synthetic line-of-sight HI velocity fields for the simulated systems, with resolution similar to that of observed galaxies, and compare the amplitudes of the harmonic modes of simulated and observed galaxies.

In order to produce synthetic HI datacubes for the 33 systems in our simulated sample, we follow a procedure sim-

ilar to that described by O17 in their Section 3.3. The procedure consists of the following steps. Assume that a system is made of  $N$  gas particles, each described by its coordinates  $(x, y, z)$ , velocities  $(V_x, V_y, V_z)$ , temperature  $T$ , and HI mass  $m_{\text{HI}}$ :

- the system is projected at  $60^\circ$  inclination, using  $\vec{L}_*$  as a reference direction, and a random orientation;
- a position-velocity 3D grid is created, with a spatial binning of  $83 \text{ pc}$  and a channel separation of  $2 \text{ km s}^{-1}$ ;
- the  $m_{\text{HI}}$  of each particle is placed at the corresponding  $(x, y)$  location in the grid, and is distributed in velocity around its  $V_z$  by using a Gaussian kernel with a standard deviation of  $\sqrt{k_{\text{B}}T/m_{\text{H}}}$ ,  $k_{\text{B}}$  being the Boltzmann constant and  $m_{\text{H}}$  the proton mass. This is to take the thermal broadening of the line profiles into account.
- once all particles have been processed, the resulting datacube is smoothed spatially at the FWHM resolution of  $250 \text{ pc}$  (three times the grid binning).

For simplicity we make no correction for gas opacity, i.e., the gas is considered to be optically thin. Note that, as in O17, the final resolution of our synthetic observations is similar to that of THINGS and LITTLE THINGS datacubes. Velocity fields are derived from these datacubes as moment-1 maps, which are well suited to account for non-circular motions in the gas kinematics.

Finally, we perform a harmonic analysis of the velocity fields for both samples. The procedure requires a careful choice of galaxy centre. For the simulated galaxies, we assume that this coincides with the location of the minimum gravitational potential, whereas for the real galaxies we take the kinematic centres estimated by Trachternach et al. (2008) for THINGS and by Oh et al. (2015) for LITTLE THINGS.

We focus on the amplitude of the  $m = 1$  and  $m = 3$  harmonic modes at two fixed galactocentric distances:  $R = 1 \text{ kpc}$  and  $R = 2 \text{ kpc}$ , which bracket the range of  $R_{\text{h}}$  in our simulated sample and are well-resolved radii in both observations and simulations. In practice, we select a ring on the galactic plane with mean radius equal to the chosen value (1 or 2 kpc) and width equal to the FWHM resolution (which varies in the sample of real galaxies, but is constant in the simulated sample). Each ring is defined by its inclination,  $i$ , and position angle, PA, in the sky.

Given that the choice of these two parameters significantly affects the outcome of the harmonic analysis, we must adopt a criterion that sets them uniquely and that can be applied to both observed and synthetic velocity fields. For any given  $(i, \text{PA})$ , the line-of-sight velocity,  $V_{\text{LOS}}$ , within the ring as a function of the azimuthal angle in the plane of the galaxy,  $\theta$ , is fit with a formula analogous to eq. (1), from which we extract the amplitudes  $A_1$ ,  $A_2$  and  $A_3$ . Our choice for  $(i, \text{PA})$  is the one that *minimises* the quantity  $\sqrt{A_2^2 + A_3^2}/|A_1|$ , which quantifies the strength of large-scale perturbations with respect to regular rotation at a given radius. The minimisation is achieved via the Nelder & Mead (1965) method.

We adopt  $(i = 60^\circ, \text{PA} = 90^\circ)$  as the initial guess for the simulated galaxies, while for the observed galaxies we use the values of  $i$  and PA determined by de Blok et al. (2008, for THINGS) and by Oh et al. (2015, for LITTLE

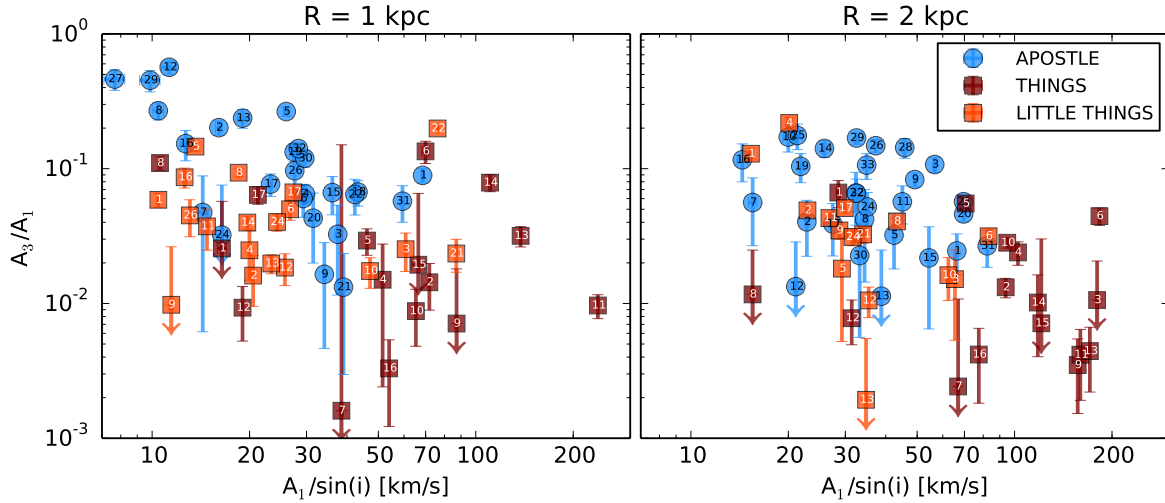


**Figure 8.** bisymmetric H I flows in simulated and observed galaxies at galactocentric radii of  $R=1$  kpc (*left panel*) and  $R=2$  kpc (*right panel*). The ratio between the amplitudes of the  $m=3$  and the  $m=1$  harmonic modes is plotted as a function of the amplitude of the  $m=1$  mode (divided by  $\sin(i)$ ) in the H I velocity fields of APOSTLE galaxies (blue circles), THINGS galaxies (brown squares), and LITTLE THINGS galaxies (orange squares). Error bars show the formal errors on the harmonic fit to the velocities. Arrows represent upper limits. Systems are numbered as in Tables A1 and A2 of O17. On average, simulated galaxies show stronger bisymmetric motions than the observed galaxies.

THINGS) from their tilted ring fitting method. Typically, the final ( $i$ , PA) determined for the observed galaxies remains within  $\sim 5^\circ$  from the initial estimates. The simulated sample, however, shows much larger deviations from the initial guess.

In some cases, fitting  $V_{\text{LOS}}$  via eq. (1) was not possible due to the small number of points, or - in observed galaxies - to an excessively noisy velocity field. For these reasons DDO 53, DDO 210, IC 10, IC 1613, NGC 1569, UGC 8508 and Haro 29 have been excluded from our analysis at  $R=1$  kpc, along with DDO 168, DDO 216, NGC 3738 and Haro 36 at  $R=2$  kpc.

Figure 8 shows the ratio between  $A_3$  and  $A_1$ , which is a measure of the strength of the bisymmetric flow with respect to regular H I rotation, as a function of  $A_1/\sin(i)$ , which represents the H I azimuthal speed  $V_\phi$  alone<sup>3</sup>, at  $R=1$  kpc (left panel) and  $R=2$  kpc (right panel) for the real (squares) and simulated (circles) galaxies.

Interestingly, there is a common trend followed by both real and simulated galaxies: the importance of non-circular motions compared to the regular rotation decreases as a function of rotation speed. The main difference between observed and simulated galaxies is in the amplitudes of the bisymmetric motions: the median  $A_3/A_1$  at  $R=1$  kpc ( $R=2$  kpc) is 0.083 (0.057) in APOSTLE, 0.017 (0.010) in THINGS and 0.040 (0.033) in LITTLE THINGS. Limiting the comparison to the LITTLE THINGS sample alone, which spans a range of  $A_1/\sin(i)$  similar to our APOSTLE sample, we conclude that bisymmetric flows in APOSTLE dwarfs are a factor  $\sim 2$  stronger than those in the observed galaxies.

We have verified that these results hold when the har-

monic analysis is performed at the effective radius  $R_{\text{eff}}$  of each system, or at  $2R_{\text{eff}}$ , rather than at a fixed galactocentric distance, using effective radii from the SPARC catalogue of Lelli et al. (2016) and the catalogue of Hunter & Elmegreen (2006).

These results suggest that bisymmetric flows caused by bar-like features, or, more generally, by asphericities in the gravitational potential are somewhat less prominent in observed galaxies than in the APOSTLE simulations, at least in the dwarf galaxy regime, in line with the earlier findings of Trachternach et al. (2008).

There are, however, important caveats in the comparison. One is that, while our analysis considers all APOSTLE galaxies in the range  $60 < V_{\text{max}}/\text{km s}^{-1} < 120$ , the observed sample has no well-defined completeness criteria. A second difference, already mentioned above, is in the velocity range covered: only 8 galaxies in the observed sample have  $60 < V_{\text{max}}/\text{km s}^{-1} < 120$ . A further difference is environmental: the APOSTLE galaxies are located in the proximity (i.e. within  $\sim 3$  Mpc) of a Local Group analogue, whereas the THINGS and LITTLE THINGS galaxies are in less dense environments. In light of these considerations, we argue that the differences in the  $A_3/A_1$  ratio shown in Figure 8, although suggestive, should be treated with caution.

## 4 CONCLUSIONS

Cold dark matter haloes are triaxial in nature (e.g. Frenk et al. 1988). Their asphericity increases towards their centre (Hayashi et al. 2007), implying that the process of galaxy formation in a  $\Lambda$ CDM framework occurs within gravitational potentials that are non axisymmetric, or, broadly speaking, ‘barred’. The processes of stellar mass assembly and secular evolution can reduce the halo triaxiality significantly in massive disc galaxies (Kazantzidis et al. 2010; Abadi et al. 2010;

<sup>3</sup> In reality,  $A_1$  is a combination of rotation and a global expansion/contraction in the radial direction, but the latter is typically negligible



Machado & Athanassoula 2010), but are much less efficient in dwarf galaxies, which therefore may be forced to respond to non-axisymmetric forces due to the dark matter.

In this work, we have carried out a study of the mass distribution and HI kinematics within the central few kiloparsecs in a sample of 33 HI-rich dwarf ( $60 < V_{\max} < 120 \text{ km s}^{-1}$ ) galaxies from the APOSTLE suite of  $\Lambda$ CDM cosmological hydrodynamical simulations. Our results can be summarised as follows:

- Most simulated dwarfs have a bar in their stellar component that matches the non-axisymmetric distribution of the inner dark matter halo ('dark' bar). Specifically, 18 out of 33 APOSTLE dwarfs (55 per cent) have a stellar and a dark bar with axis ratios smaller than 0.85.
- When present, the stellar and the dark bar co-rotate and are locked in phase.
- Since the gravitational potential is dominated by the dark matter, the stellar bar follows the dark bar, not vice-versa. A corollary is that the presence of a stellar bar does not imply that baryons dominate gravitationally that region.
- All bars in the sample analysed are weak, and have co-rotation radii that largely exceed the galaxy size.
- The stellar/dark bar induces significant bisymmetric flows in the gas component. We have compared the amplitude of the  $m=3$  harmonic perturbations in the HI velocity fields of the APOSTLE systems with those of THINGS and LITTLE THINGS galaxies, finding that the magnitude of bisymmetric flows in the former exceeds that in the latter by a factor of  $\sim 2$ .

Our findings clarify the nature of the non-circular motions reported by O17 in the same simulated galaxy sample as due to the effects of a dominant triaxial halo. Our analysis also shows that, although halos are sphericalised by the assembly of the galaxy, the sphericalisation is incomplete in dwarfs like the ones in our APOSTLE sample. The remaining triaxiality induces the formation of a bar-like feature in the stars and non-circular motions in the gas. Although the magnitude of such motions seems to exceed, on average, those in galaxies of the THINGS and LITTLE THINGS surveys, we caution that these surveys are not exactly comparable, so a definitive conclusion about whether our findings are in agreement or disagreement with real galaxies in the local Universe remains pending and will be the focus of future work.

## ACKNOWLEDGEMENTS

The authors thank the THINGS, LITTLE THINGS and SPARC survey teams for making their data publicly available. AM thanks Mattia Sormani for helpful discussions. CSF acknowledges support from ERC Advanced Grant 267291 Cosmiway. This work used the DiRAC Data Centric system at Durham University, operated by the Institute for Computational Cosmology on behalf of the STFC DiRAC HPC Facility ([www.dirac.ac.uk](http://www.dirac.ac.uk)). This equipment was funded by BIS National E-infrastructure capital grant ST/K00042X/1, STFC capital grant ST/H008519/1, and STFC DiRAC Operations grant ST/K003267/1 and Durham University. DiRAC is part of the National E-Infrastructure.

## REFERENCES

- Abadi M. G., Navarro J. F., Fardal M., Babul A., Steinmetz M., 2010, *MNRAS*, **407**, 435
- Agertz O., et al., 2007, *MNRAS*, **380**, 963
- Algorry D. G., et al., 2017, *MNRAS*, **469**, 1054
- Athanassoula E., 1992, *MNRAS*, **259**, 328
- Athanassoula E., 2002, *ApJ*, **569**, L83
- Athanassoula E., 2003, *MNRAS*, **341**, 1179
- Athanassoula E., 2013, Bars and secular evolution in disk galaxies: Theoretical input. p. 305
- Blitz L., Rosolowsky E., 2006, *ApJ*, **650**, 933
- Cheung E., et al., 2013, *ApJ*, **779**, 162
- Contopoulos G., Grosbol P., 1989, *A&A Rev.*, **1**, 261
- Crain R. A., et al., 2015, *MNRAS*, **450**, 1937
- Crain R. A., et al., 2017, *MNRAS*, **464**, 4204
- Cullen L., Dehnen W., 2010, *MNRAS*, **408**, 669
- Dalla Vecchia C., Schaye J., 2012, *MNRAS*, **426**, 140
- de Blok W. J. G., Walter F., Brinks E., Trachternach C., Oh S.-H., Kennicutt Jr. R. C., 2008, *AJ*, **136**, 2648
- Dolag K., Borgani S., Murante G., Springel V., 2009, *MNRAS*, **399**, 497
- Durier F., Dalla Vecchia C., 2012, *MNRAS*, **419**, 465
- Fattahi A., et al., 2016, *MNRAS*, **457**, 844
- Frenk C. S., White S. D. M., Davis M., Efstathiou G., 1988, *ApJ*, **327**, 507
- Frenk C. S., Evrard A. E., White S. D. M., Summers F. J., 1996, *ApJ*, **472**, 460
- Hayashi E., Navarro J. F., 2006, *MNRAS*, **373**, 1117
- Hayashi E., Navarro J. F., Springel V., 2007, *MNRAS*, **377**, 50
- Hockney R. W., Hohl F., 1969, *AJ*, **74**, 1102
- Hunter D. A., Elmegreen B. G., 2006, *ApJS*, **162**, 49
- Hunter D. A., et al., 2012, *AJ*, **144**, 134
- Janz J., et al., 2012, *ApJ*, **745**, L24
- Jenkins A., 2013, *MNRAS*, **434**, 2094
- Jing Y. P., Suto Y., 2002, *ApJ*, **574**, 538
- Kaufmann T., Mayer L., Wadsley J., Stadel J., Moore B., 2006, *MNRAS*, **370**, 1612
- Kazantzidis S., Abadi M. G., Navarro J. F., 2010, *ApJ*, **720**, L62
- Komatsu E., et al., 2011, *ApJS*, **192**, 18
- Kormendy J., Kennicutt Jr. R. C., 2004, *ARA&A*, **42**, 603
- Lelli F., McGaugh S. S., Schombert J. M., 2016, *AJ*, **152**, 157
- Machado R. E. G., Athanassoula E., 2010, *MNRAS*, **406**, 2386
- Masters K. L., et al., 2011, *MNRAS*, **418**, 1055
- Méndez-Abreu J., Sánchez-Janssen R., Aguerri J. A. L., 2010, *ApJ*, **711**, L61
- Méndez-Abreu J., Sánchez-Janssen R., Aguerri J. A. L., Corsini E. M., Zarattini S., 2012, *ApJ*, **761**, L6
- Miller R. H., Prendergast K. H., 1968, *ApJ*, **151**, 699
- Mulchaey J. S., Regan M. W., 1997, *ApJ*, **482**, L135
- Nelder J. A., Mead R., 1965, *The Computer Journal*, **7**, 308
- Oh S.-H., et al., 2015, *AJ*, **149**, 180
- Oman K. A., Marasco A., Navarro J. F., Frenk C. S., Schaye J., Benítez-Llambay A., 2017, preprint, ([arXiv:1706.07478](https://arxiv.org/abs/1706.07478))
- Ostriker J. P., Peebles P. J. E., 1973, *ApJ*, **186**, 467
- Power C., Navarro J. F., Jenkins A., Frenk C. S., White S. D. M., Springel V., Stadel J., Quinn T., 2003, *MNRAS*, **338**, 14
- Price D. J., 2008, *Journal of Computational Physics*, **227**, 10040
- Rahmati A., Pawlik A. H., Raicevic M., Schaye J., 2013, *MNRAS*, **430**, 2427
- Sawala T., et al., 2015, *MNRAS*, **448**, 2941
- Schaller M., Frenk C. S., Fattahi A., Navarro J. F., Oman K. A., Sawala T., 2016, *MNRAS*, **461**, L56
- Schaye J., Dalla Vecchia C., 2008, *MNRAS*, **383**, 1210
- Schaye J., Crain R. A., Bower R. G., Furlong M., Schaller M. e. a., 2015, *MNRAS*, **446**, 521
- Schoenmakers R. H. M., Franx M., de Zeeuw P. T., 1997, *MNRAS*, **292**, 349

- Sellwood J. A., 2014, [Reviews of Modern Physics](#), **86**, 1
- Sellwood J. A., Wilkinson A., 1993, [Reports on Progress in Physics](#), **56**, 173
- Spekkens K., Sellwood J. A., 2007, [ApJ](#), **664**, 204
- Trachternach C., de Blok W. J. G., Walter F., Brinks E., Kennicutt Jr. R. C., 2008, [AJ](#), **136**, 2720
- Walter F., Brinks E., de Blok W. J. G., Bigiel F., Kennicutt Jr. R. C., Thornley M. D., Leroy A., 2008, [AJ](#), **136**, 2563
- Warren M. S., Quinn P. J., Salmon J. K., Zurek W. H., 1992, [ApJ](#), **399**, 405
- Wiersma R. P. C., Schaye J., Smith B. D., 2009a, [MNRAS](#), **393**, 99
- Wiersma R. P. C., Schaye J., Theuns T., Dalla Vecchia C., Tornatore L., 2009b, [MNRAS](#), **399**, 574

This paper has been typeset from a  $\text{T}_{\text{E}}\text{X}/\text{L}^{\text{A}}\text{T}_{\text{E}}\text{X}$  file prepared by the author.